

MRI-Powered Robotics

Aaron T. Becker and Ouajdi Felfoul and Li Huang and Pierre E. Dupont

Abstract MRI-based navigation and propulsion of millirobots is a new and promising approach for minimally invasive therapies. The strong central field inside the scanner, however, precludes torque-based control. Consequently, prior propulsion techniques have been limited to gradient-based pulling through fluid-filled body lumens. This paper introduces a technique for generating large impulsive forces that can be used to penetrate tissue. The approach is based on navigating multiple robots to a desired location and using self-assembly to trigger the conversion of magnetic potential energy into sufficient kinetic energy to achieve penetration. The approach is illustrated through analytical modeling and experiments in a clinical MRI scanner.

1 Introduction

Robotics offers important contributions to image-guided, minimally invasive surgery. Among imaging techniques, MRI has several advantages. MRI provides high resolution soft-tissue imaging and does not use ionizing radiation.

MR image-guided procedures, however, pose several challenges for robotics [2, 3, 4, 5, 6]. First, all ferrous materials create imaging artifacts. Ferrous materials must be isolated from the imaging region of interest. Moreover, the magnetic fields used in an MRI induce forces on any ferrous materials in the robot and turn these materials into strong magnetic dipoles that exert forces on each other. MRI gradients induce current in any conducting materials, which can generate dangerous amounts of heat and also exert forces.

Aaron T. Becker and Li Huang

Department of Electrical and Computer Engineering, University of Houston, Houston, TX 77004, USA, e-mail: atbecker@uh.edu, e-mail: lhuang28@uh.edu

Ouajdi Felfoul and Pierre E. Dupont

Department of Cardiovascular Surgery, Boston Children's Hospital and Harvard Medical School, Boston, MA, 02115 USA e-mail: firstname.lastname@childrens.harvard.edu

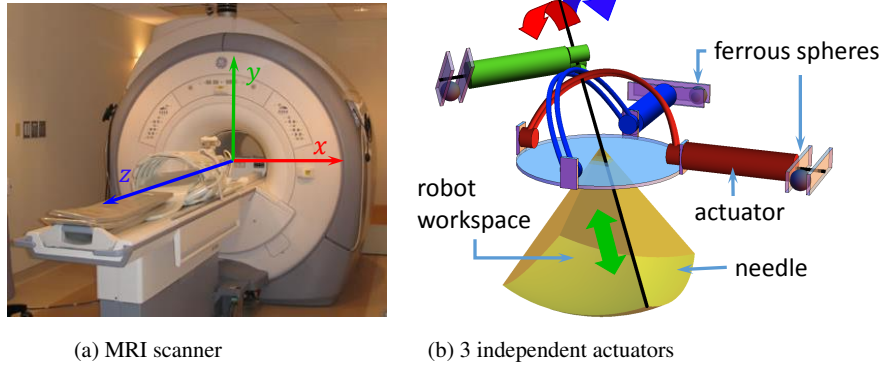


Fig. 1 n non-parallel rotors can be independently actuated by the same magnetic gradient field. The torque from these rotors could power multi-DOF robotic actuators running untethered inside an MRI bore such as (b), a biopsy robot inspired by [1] that can insert a needle and tilt the needle to a two DOF compound angle.

Despite these challenges, there are a number of recent innovations demonstrating tetherless and inexpensive actuation imaged, powered, and controlled using MRI. Martel et al. demonstrated in vivo motion control of a mm-scale particle in the carotid artery of swine [4]. Vartholomeos et al. designed a single-DOF MRI-powered actuator for use as a tetherless biopsy robot [5]. This was extended to closed-loop control of a single rotor in [6]. Since such results require only scanner software and inexpensive actuator components, dissemination of MRI-based robotic technology has the potential to be rapid and inexpensive.

While this prior work has demonstrated control of a single particle or a single rotor, many clinical applications require multiple DOF. This is a challenge because the three orthogonal magnetic gradients of MRI scanners are applied over the entire scanner bore, so the resulting control problem is underactuated. Techniques from nonlinear control theory must be used to demonstrate controllability and to derive control laws.

Millimeter-scale robots have the potential to provide highly localized therapies with minimal trauma by navigating through the natural fluid-filled passageways of the body. While navigation through, e.g., the circulatory system or cerebrospinal fluid spaces, is sufficient for some applications, it can also be necessary to penetrate into the surrounding tissue. Examples include puncturing a membrane to release trapped fluid, opening a blocked passageway or delivering a drug to a tissue location several centimeters from a fluid-filled space. The forces required for tissue penetration, however, are substantially higher than those needed to propel a millirobot through a bodily fluid and, consequently, can be difficult to achieve. Prior tetherless systems for moving through tissue have relied on magnetic forces and torques produced by large external magnets to either pull magnetic spheres through brain tissue [7] or to rotate threaded magnetic cylinders through muscle tissue [?].

Alternatively, methods for tetherless robot propulsion and control have been developed that employ the magnetic gradients of clinical MRI scanners [8, 9, 6, 10]. MRI also provides the capability to image both the robot and surrounding tissue to guide navigation. MRI-based millirobot navigation in the vasculature was first demonstrated in [8]. Recently, algorithms enabling the simultaneous MRI-based control of multiple millirobots [9, ?] and macro-scale rotary actuators [6, 10] have also been developed.

To date, however, the motion of MRI-powered millirobots has been constrained to fluid-filled spaces since the magnetic gradients produced by the scanner are relatively weak. The maximum gradient produced by most clinical scanners is in the range of 20-40mT/m producing a force on a magnetized steel particle equal to 36-71% of its gravitational force. While it is possible to install custom high-strength gradient coils, such as the 400mT/m coil reported in [?], this approach is costly and can reduce the size of the MRI bore. While to facilitate motion within a fluid, a millirobot can be designed to be neutrally buoyant, the force magnitude produced by the magnetic gradient is not capable of producing tissue penetration.

In an MRI scanner, there is no need for permanent magnets, since steel is highly magnetized by the 3T magnetic field of an MRI. Each stage, containing two magnetized spheres separated by a nonmagnetic spacer, is individually stable. Using existing control approaches [9, ?], they can be navigated through fluid-filled spaces and self-assembled at a desired penetration location. The assembly can then be fired by a special trigger module consisting of two spheres separated by a spacer longer than that used in the individual stages. After firing, the assembly can be navigated out of the body.

what is our contribution? The contribution of this paper is to develop control techniques enabling independent control of large numbers of rotors. Section ?? describes an MRI actuator model and a multi-rotor control law. Section ?? examines multi-actuator system optimization. Section ?? applies these principles to design a 3 DOF biopsy robot (Fig. 1), and Section ?? ends with concluding remarks.

2 Theory

Ferrous material placed inside the strong B_0 field of an MRI become strong magnets. This section describes the forces and torques these magnets exert on other magnets, the magnetic potential energy between these magnets, and how this energy is exploited in a Gauss gun.

2.1 Magnet Interaction Forces

Any ferrous material placed in the magnetic field of an MR scanner becomes a strong magnetic dipole. The gradient fields can then apply forces on these dipoles.

Additionally, the dipoles exert forces on each other. Dipole forces overpower MRI gradient forces if the materials are closer than a threshold distance.

The magnetic field at position \mathbf{p}_2 generated by a spherical magnet at position \mathbf{p}_1 with magnetization \mathbf{m}_1 is [11]

$$\mathbf{B}_{\mathbf{p}_1}(\mathbf{p}_2) = \frac{\mu_0}{4\pi} \frac{3\mathbf{n}_{12}(\mathbf{n}_{12} \cdot \mathbf{m}_1) - \mathbf{m}_1}{|\mathbf{p}_2 - \mathbf{p}_1|^3}, \quad (1)$$

with $\mathbf{n}_{12} = (\mathbf{p}_2 - \mathbf{p}_1)/|\mathbf{p}_2 - \mathbf{p}_1|$. This is the *magnetic field of a dipole*. The force applied to a dipole at \mathbf{p}_1 with magnetic moment \mathbf{m}_1 by another dipole at \mathbf{p}_2 with magnetic moment \mathbf{m}_2 is approximated by

$$\mathbf{F}_{12} \approx \frac{3\mu_0}{4\pi} \frac{1}{|\mathbf{p}_2 - \mathbf{p}_1|^4} \left[5\mathbf{n}_{12} \left((\mathbf{m}_1 \cdot \mathbf{n}_{12})(\mathbf{m}_2 \cdot \mathbf{n}_{12}) \right) - \mathbf{n}_{12}(\mathbf{m}_2 \cdot \mathbf{m}_1) - \mathbf{m}_1(\mathbf{m}_2 \cdot \mathbf{n}_{12}) - \mathbf{m}_2(\mathbf{m}_1 \cdot \mathbf{n}_{12}) \right]. \quad (2)$$

The torque applied on a dipole at \mathbf{p}_2 by a dipole at \mathbf{p}_1 is

$$\boldsymbol{\tau}_{12} = \mathbf{m}_2 \times \mathbf{B}_{\mathbf{p}_1}(\mathbf{p}_2) \quad (3)$$

Inside a 3T MRI, a steel sphere becomes fully magnetized with magnetic saturation $M_s = 1.36 \times 10^6$. The magnetic moment of a sphere with radius r_{sphere} is aligned with the MRI B_0 field:

$$\mathbf{m}(r_{sphere}) = \begin{bmatrix} 0 \\ 0 \\ 1 \end{bmatrix} \frac{4}{3} \pi r_{sphere}^3 M_s. \quad (4)$$

Figure 4 shows contour plots for the magnetic force exerted by two identical spheres on each other. The contour lines show $\mathbf{F} \cdot \mathbf{n}_{12}$, the force component radially outward from the sphere at $(0,0)$ compared to the maximum force provided by the gradient coils g_M . This force is attractive (red) along the z -axis and repulsive (blue) perpendicular to z . The magnetic field is symmetric about the z -axis. If two spheres move within the dark red region, they cannot be separated using the gradient field. The contour lines are drawn at $\mathbf{F}_{12} \cdot \mathbf{n}_{12} = g_M \cdot \{-1, -\frac{1}{10}, 0, \frac{1}{10}, 1\}$. The maximum force is along the z -axis

$$F_{\text{attraction}} = -\frac{8M_s^2 \mu_0 \pi r_1^3 r_2^3}{3d^4}, \quad (5)$$

where d is the distance separating two spheres of radii r_1 and r_2 , each with magnetic saturation M_s . The vacuum permeability μ_0 is, by definition, $4\pi \times 10^{-7} \text{ V} \cdot \text{s}/(\text{A} \cdot \text{m})$.

The critical distance when the attractive force becomes greater than the maximum gradient force is $\sqrt[4]{\frac{2M_s \mu_0 r_{sphere}^3}{g_M}}$.

3 Related Work

We can use parts of our TRO paper for the related work.

Copy in content from related work section of <https://github.com/aabecker/MRIrobotics/tree/master/Papers-Current/MRIMultiOrthoRotors>

Copy in content from related work section <https://github.com/aabecker/MRIrobotics/tree/master/Papers-Current/GaussGun>

3.1 Robot Actuators

The magnetic gradient from an MRI can be harnessed to power and control centimeter-scale motors. (we could finally cite the Japanese people); Contrast with piezo electric, ultrasonic, pneumatic, etc.

Long history of Pierre's lab, culminate with recent TOR paper
Mention the Straandbeast

3.2 Particle Manipulation

MRI: beads: Pierre, Christos, Martel,

3.3 Milli-Robots

anything with multiple components/engineered components: MRI-millirobots, Gabor's flagella, gauss-gun, Martel's swimmers with tails, etc.

4 Case Study 1: Multiple Rotor Control

Copy in content from <https://github.com/aabecker/MRIrobotics/tree/master/Papers-Current/MRIMultiOrthoRotors>

While this prior work has demonstrated control of a single particle or a single rotor, many clinical applications require multiple DOF. This is a challenge because the three orthogonal magnetic gradients of MRI scanners are applied over the entire scanner bore, so the resulting control problem is underactuated. Techniques from nonlinear control theory must be used to demonstrate controllability and to derive control laws. The contribution of this paper is to develop control techniques enabling independent control of large numbers of rotors.

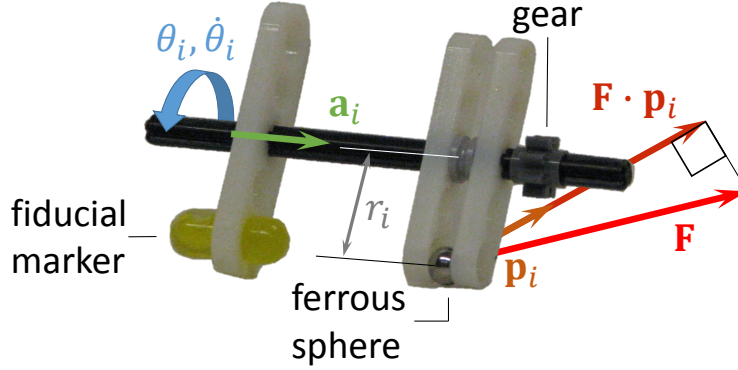


Fig. 2 MRI-powered, single-DOF rotor with gear for power transmission.

This paper investigates rotors that constrain the i th ferromagnetic sphere to rotate about an axis \mathbf{a}_i with a moment arm of length r_i , as shown in Fig. 2. The rotor's configuration is fully described by its angular position and velocity $[\theta_i, \dot{\theta}_i]^\top$. The configuration space of all n rotors is $\mathbb{R}^{2 \times n}$.

There are two standard actuator control tasks: position and velocity control. The position control problem is to find inputs $\mathbf{F}(t)$ such that for any $\boldsymbol{\theta}(0)$ and $\boldsymbol{\theta}_{\text{goal}}$,

$$\lim_{t \rightarrow \infty} \sum_{i=1}^n \left\| \begin{bmatrix} \theta_i(t) \\ \dot{\theta}_i(t) \end{bmatrix} - \begin{bmatrix} \theta_{\text{goal},i} \\ 0 \end{bmatrix} \right\|_2 = 0. \quad (6)$$

This section starts with the simpler velocity control problem

$$\lim_{t \rightarrow \infty} \sum_{i=1}^n \|\dot{\theta}_i(t) - \omega_i\|_2 = 0, \quad (7)$$

where $\omega_i \in \mathbb{R}$ is the desired angular velocity of each rotor. After solving the velocity control problem in Sec. ??, Section ?? uses an outer control loop to stabilize position.

To enable robust, multi-axis control, a closed-loop controller can be designed using a control-Lyapunov function [12]. The control law selects the three magnetic gradients that decrease the sum of squared velocity error. There are configurations where no combination of velocity gradients will decrease this error, but it is always possible to apply a non-zero gradient without increasing the sum squared error. Any non-zero gradient will move the rotors to a new configuration where the error can be decreased.

Given n non-parallel rotors and desired angular velocities ω_i , a suitable Lyapunov function can be defined as the sum squared velocity error:

$$V(\boldsymbol{\theta}, \dot{\boldsymbol{\theta}}, t) = \frac{1}{2} \sum_{i=1}^n (\omega_i - \dot{\theta}_i(t))^2 \quad (8)$$

$$\begin{aligned}\dot{V}(\boldsymbol{\theta}, \dot{\boldsymbol{\theta}}, t) &= \sum_{i=1}^n (\omega_i - \dot{\theta}_i(t)) \ddot{\theta}_i(t) \\ &= \mathbf{F}(t) \cdot \sum_{i=1}^n (\omega_i - \dot{\theta}_i(t)) \frac{r_i}{J_i} \mathbf{p}_i(t)\end{aligned}\quad (9)$$

The following controller makes $\dot{V}(\boldsymbol{\theta}, \dot{\boldsymbol{\theta}}, t)$ negative semi-definite:

$$\begin{aligned}\mathbf{f} &= \text{sgn} \left(- \sum_{i=1}^n (\omega_i - \dot{\theta}_i(t)) \frac{r_i}{J_i} \mathbf{p}_i(t) \right) \\ \mathbf{F}(t) &= g_M v_i M_{sz} \begin{cases} [1, 1, 1]^\top & \text{if } \mathbf{f} = 0 \text{ and } \dot{\boldsymbol{\theta}} \neq \boldsymbol{\omega} \\ \mathbf{f} & \text{else} \end{cases}\end{aligned}\quad (10)$$

This ensures that the system is asymptotically stable.

Position control is possible by implementing a feedback loop around (10) with a time-varying $\boldsymbol{\omega}(t)$. Given a desired position vector $\boldsymbol{\theta}_{\text{goal}}$, a PID controller can be implemented to determine $\boldsymbol{\omega}(t)$ based on the position error vector, \mathbf{e} :

$$\begin{aligned}\mathbf{e}(t) &= \boldsymbol{\theta}_{\text{goal}} - \boldsymbol{\theta}(t) \\ \boldsymbol{\omega}(t) &= K_p \mathbf{e}(t) + K_i \int_0^t \mathbf{e}(\tau) d\tau + K_d \frac{d}{dt} \mathbf{e}(t).\end{aligned}\quad (11)$$

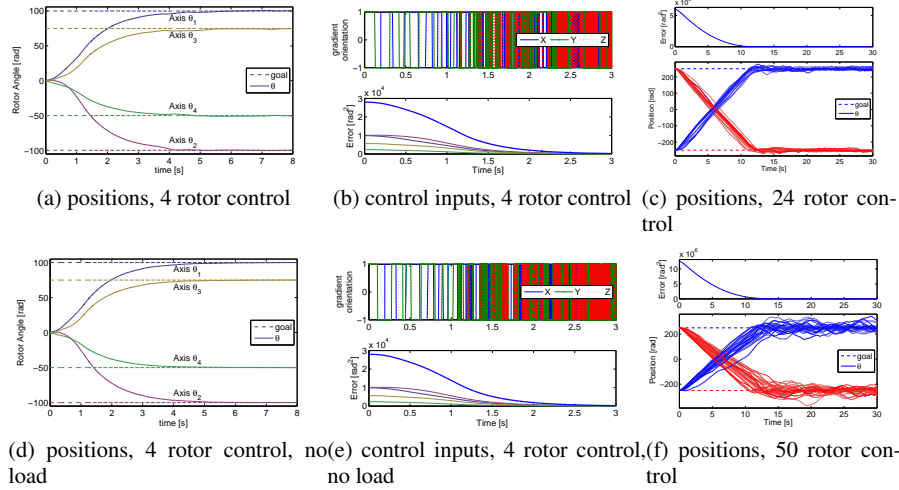


Fig. 3 Simulated position control of multiple non-parallel rotors.

The preceding section demonstrated how closed-loop control can independently control multiple rotors. Given this capability, there are constraints that must be respected when designing an MRI powered and controlled multi-actuator system. These involve (1) arranging the rotors to minimize interaction forces, (2) MRI

imaging-based tracking of each rotor, (3) geometrically arranging the rotor axes to maximize torque, and (4) calculating the stall torque as a function of the number of actuators. Each of these is described below.

Any ferrous material placed in the magnetic field of an MR scanner becomes a strong magnetic dipole. With multiple MR-powered motors, these dipoles exert forces on each other. Dipole forces overpower MRI gradient forces if rotors are closer than a threshold distance.

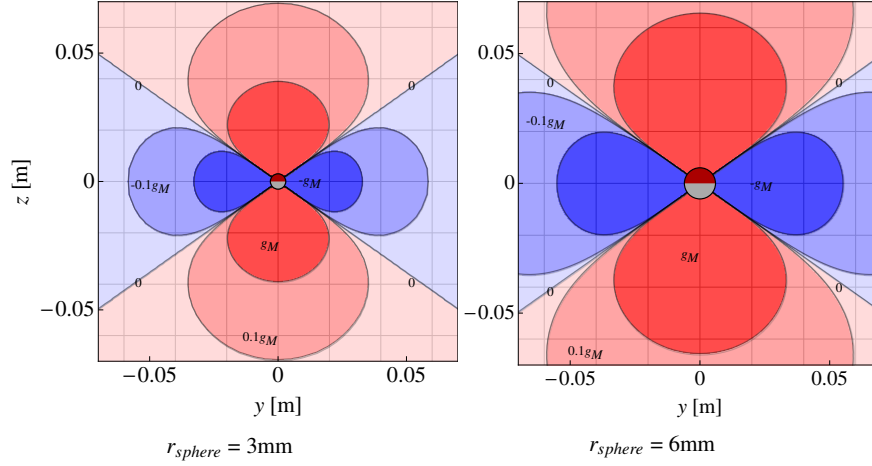


Fig. 4 One ferrous sphere in a 3T magnetic field exerts a force \mathbf{F} on an identical sphere. The contour lines show $\mathbf{F} \cdot \mathbf{n}_{12}$, the force component radially outward from the sphere at $(0,0)$ compared to the maximum force provided by the gradient coils g_M . This force is attractive (red) along the z -axis and repulsive (blue) perpendicular to z . The magnetic field is symmetric about the z -axis. If two spheres move within the dark red region, they cannot be separated using the gradient field.

Figure 4 shows contour plots for the magnetic force exerted by two identical spheres on each other. The contour lines are drawn at $\mathbf{F}_{12} \cdot \mathbf{n}_{12} = g_M \cdot \{-1, -\frac{1}{10}, 0, \frac{1}{10}, 1\}$. Rotors with spheres closer than the g_M contour lines will become stuck because they experience a force greater than what the gradient can exert. The maximum force is along the z -axis, and the critical distance when the attractive force becomes greater than the maximum gradient force is $\sqrt[4]{\frac{2\mathbf{M}_s\mu_0r_{sphere}^3}{g_M}}$. This interaction decays quickly and at distance $\approx 5.4r_{sphere}^{3/4}$ is 10% of the maximum gradient. The required distance, d , to ensure dipole-dipole forces are less than some *percentage* of the maximum gradient is given by

Localizing several rotors is difficult because their projections can overlap. One method to avoid overlapping signals uses unique distances between marker and ferrous sphere on each rotor. By appropriate choice of offset resonance frequency and its bandwidth, only one rotor at a time is visible on any acquired projection. However, this method requires an additional tracking sequence for each rotor.

A faster alternative is to design the rotors and projections so the paths of the markers do not intersect in any projection. In this way, n rotors can be simulta-

neously tracked with a single acquisition sequence, followed by detecting n non-intersecting peaks on each projection. This approach is illustrated in Fig. 5, showing three orthogonal projections for tracking three orthogonal rotors. This tracking sequence requires 25ms, enabling real-time positioning of the rotors. For this method to work, each marker must be disjoint in at least two non-parallel projections, and these projections must not be parallel with the axis of rotation. Reconstructed rotor positions from an experiment with three parallel rotors are depicted in Fig. 6.

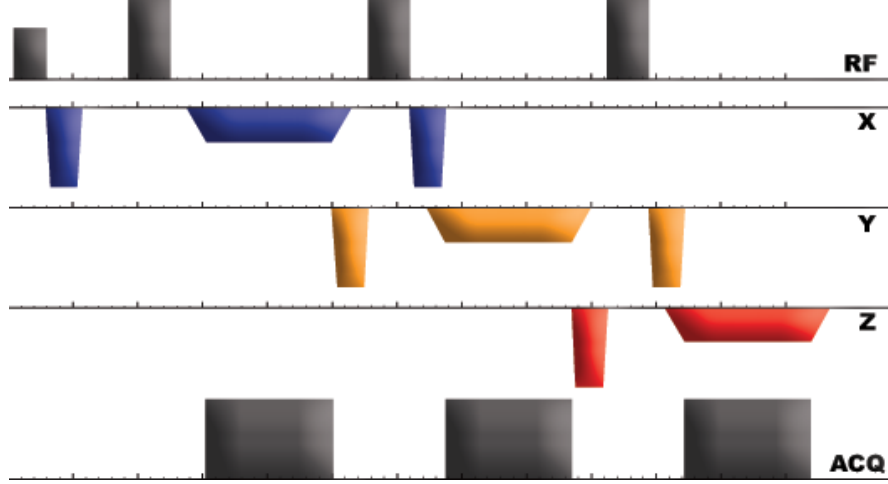


Fig. 5 MRI Fast Spin Echo sequence for tracking three orthogonal rotors.

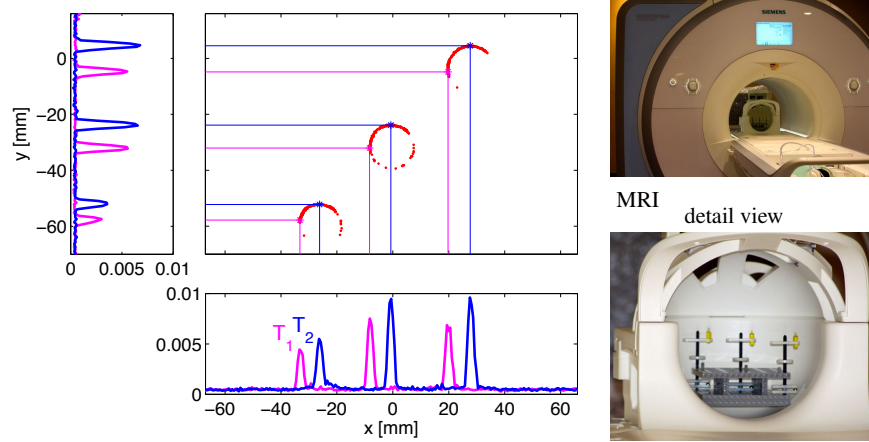


Fig. 6 Simultaneous tracking of three rotors with two line scans.

Controllability depends on both the geometric arrangement and the physical properties of the rotors, e.g. $\theta_i(0), r_i, v_i$. Because the physical properties are cho-

sen to meet torque requirements, this section focuses on maximizing controllability via arranging the rotor axes of rotation.

Controller (10) exploits inhomogeneity between motor rotors. Inhomogeneity is maximized geometrically when the axes' orientations are *well spaced*, that is all axes are as far from being parallel as possible. Section ?? shows that well-spaced axes maximize output torque. Fortuitously, if the rotors are arranged on the surface of a hemisphere, well-spaced axes are also maximally separated. This minimizes the dipole-dipole forces described in Sec. ??.

This problem is a variant of the Thomson problem [13] which determines the minimum energy configuration for n electrons confined to the surface of a sphere. In this variant, to each of the n electrons located at $\mathbf{a}_i \in \mathbb{R}^3, \|\mathbf{a}_i\|_2 = 1$, an additional electron at $-\mathbf{a}_i$ is bound, and the system is solved to minimize the total energy. As in the original Thomson problem, minimal energy configurations can be rigorously identified in only a handful of cases. Instead, as in [14], this paper uses numerical optimization methods to find locally optimal solutions.

The optimization problem is

$$\begin{aligned} & \underset{\mathbf{a}_1, \mathbf{a}_2, \dots, \mathbf{a}_n}{\text{minimize}} \sum_{i \neq j} \frac{1}{\|\mathbf{a}_i - \mathbf{a}_j\|_2^2} + \frac{1}{\|\mathbf{a}_i + \mathbf{a}_j\|_2^2} \\ & \text{subject to } \mathbf{a}_i \in \mathbb{R}^3, \|\mathbf{a}_i\|_2 = 1, 1 \leq i \leq n. \end{aligned} \quad (12)$$

Two effects must be considered when computing stall torque. The first is related to the directionality of the maximum gradient that can be produced by a scanner. The magnetic gradients in the three coordinate directions are produced by three separate coils and amplifiers. The maximum gradient that can be applied in each direction depends on the maximum current that each coil is designed to handle. The practical implication is that the maximum gradient that can be generated is not directed along one of the three principal coordinate axes, but occurs off-axis when the three gradient coils are all producing their maximum values. The result is that, for any given rotor axis, the maximum torque varies cyclically with rotation angle. *somewhat similar to the last optimal geometric arrangement of n rotors* The second effect arises because control effort must be divided among many rotors. This section analyzes the average torque produced with 1, 2, 3, or n rotors and how geometrically arranging the rotor axes modifies this torque.

c and p problems occurred

n rotors

With n rotors, the average stopped torque is calculated by integrating over each angle θ_i and dividing by n :

$$\bar{\tau}_n = \frac{1}{n} \frac{1}{(2\pi)^n} \underbrace{\int_0^{2\pi} \dots \int_0^{2\pi}}_n \sum_{i=1}^n \tau_i d\theta_1 \dots d\theta_n \quad (13)$$

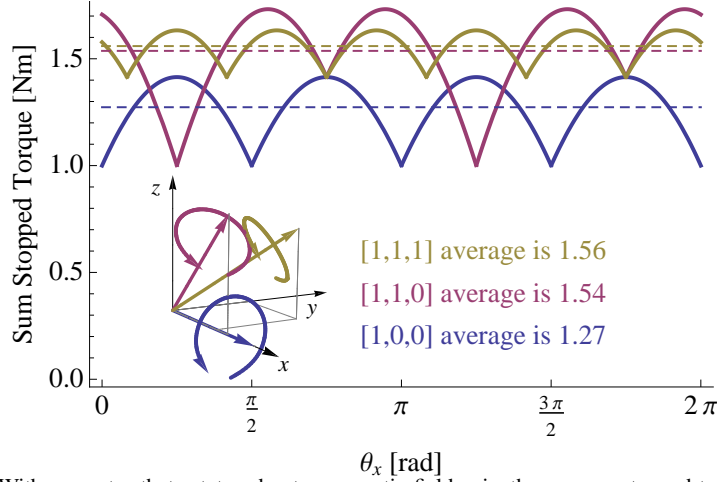


Fig. 7 With one rotor that rotates about a magnetic-field axis, the average stopped torque is $\frac{4}{\pi}$, with minimum 1 and maximum $\sqrt{2}$. Rotating about the vector $[1, 1, 0]$ or $[1, 1, 1]$ generates slightly larger average torques.

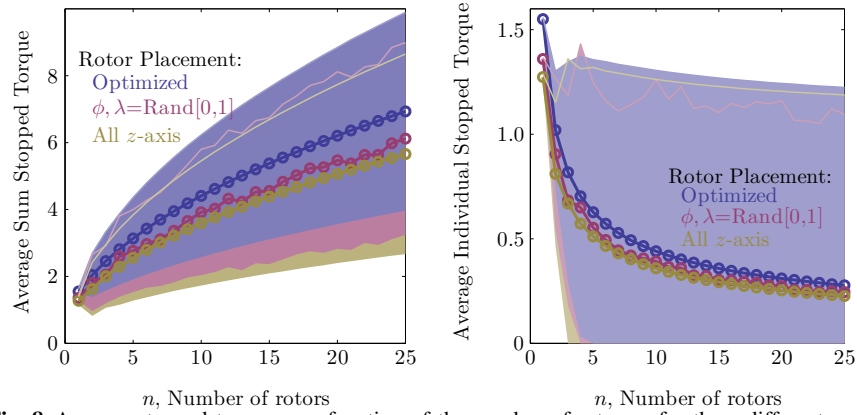


Fig. 8 Average stopped torque as a function of the number of rotors n for three different axes placement strategies. The sum torque increases sublinearly with n . The scale is normalized so 1 is the maximum torque a single gradient could impart on one rotor. Mean and \pm one standard deviation are plotted. The *optimized* placement strategy has the highest average torque.

using the numerical optimization from Section ?? generates the largest average stopped torque.

To study the preceding topics in the context of a practical example system, a three-axis biopsy robot powered by DC motors is considered [1].

Figure 1 is a schematic of the proposed system. The system has a fixed base that is attached to the patient. Two actuators, θ_x and θ_y , control orthogonal axes of a nested spherical yoke. A carriage rides along the intersection of this yoke. Mounted on this carriage is a third actuator, θ_{needle} , that can insert a needle through a pivot point at the center of the base. The original design allows θ_x and θ_y to rotate between $[-\pi/6, \pi/6]$, and inserts θ_{needle} from $[0, 100]$ mm, resulting in a spherical

quadrilateral workspace with volume $(\theta_{needle})^3 \pi/9$. The base has diameter 100m, and the nested yokes have radii 50mm.

Minimize Actuator Interaction Forces

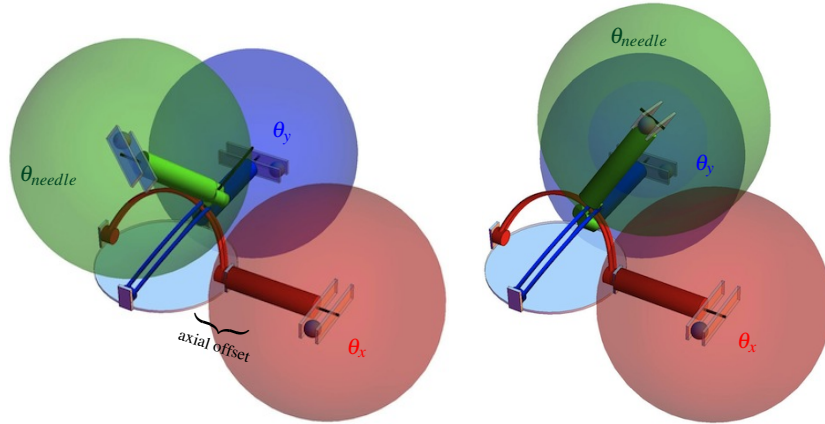


Fig. 9 Candidate designs and dipole-interaction. Spheres represent minimum separation constraint. The design at right violates the constraint.

Simultaneous Rotor Tracking

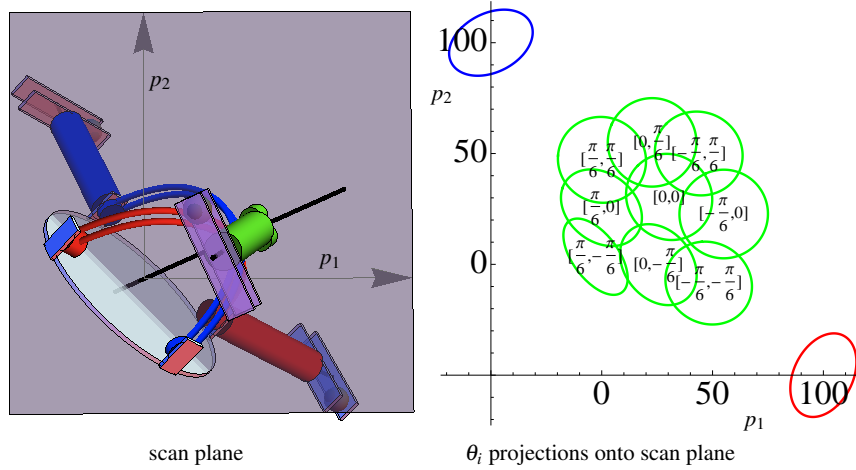


Fig. 10 All three rotors can be localized with two orthogonal line scans. These line scans can be selected such that the ellipses parameterized by θ_i are disjoint for all configurations $[\theta_x, \theta_y]$.

MRI-based multi-rotor control poses both control-theoretic challenges and practical implementation issues. To address these, this paper has provided an optimization scheme for rotor placement and derived a globally asymptotically stabilizing controller for n actuators. Both a velocity controller (10) and a position controller (11) were implemented. MATLAB implementations of these controllers are available at [15].

These controllers exploit inhomogeneities in rotor axis orientation. Constructing motors with axes that are not parallel requires careful balancing of the rotor shafts. However, it is not necessary for the rotors to be non-parallel. Ongoing research indicates that the proposed control law can also stabilize parallel rotor shafts using other inhomogeneities, e.g. $r_i, \theta_i(0), v_i$. If all axes are parallel to the gravity vector, gravity no longer interferes with rotor movement. This makes counterweights unnecessary, and allows using extremely low-friction jewel bearings since axes are not under radial load.

5 Case Study 2: Gauss Gun

Copy in content from <https://github.com/aabecker/MRIrobotics/tree/master/Papers-Current/GaussGun> To date, however, the motion of MRI-powered millirobots has been constrained to fluid-filled spaces since the magnetic gradients produced by the scanner are relatively weak. While to facilitate motion within a fluid, a millirobot can be designed to be neutrally buoyant, the force magnitude produced by the magnetic gradient is not capable of producing tissue penetration.

Need some examples to illustrate that gradient forces are not enough for tissue penetration (challenges). Like the following part

Consider, for example, that a standard 18 gauge needle requires 0.59 ± 0.11 N of force to penetrate 10mm into muscle tissue [16]. Bioinspired design can somewhat reduce these forces, e.g., the backward-tipped barbs of the North American porcupine quill exhibit forces of 0.33 ± 0.08 N for 10mm of muscle penetration [16]. Nevertheless, to reproduce even these forces using an MRI with a steel needle would require a 3.3m long shaft – longer than the bore of the scanner. While the size of macro-scale MRI-based actuators permits the use of gear transmissions to trade off velocity and force [9, ?], this approach is not feasible at the millimeter scale. Therefore, to address the challenge of MRI-based tissue penetration, an alternative to gradient-based force production is needed.

The observation that tissue puncture force is inversely related to penetration velocity [17] motivates the concept of using energy storage and sudden release to perform penetration. The concept, illustrated in Fig. 11, corresponds to a Gauss gun or accelerator [18, 19]. In an MRI scanner, there is no need for permanent magnets, since steel is highly magnetized by the 3T magnetic field of an MRI. Each stage, containing two magnetized spheres separated by a nonmagnetic spacer, is individually stable. Using existing control approaches [9, ?], they can be navigated through fluid-filled spaces and self-assembled at a desired penetration location. The assem-

bly can then be fired by a special trigger module consisting of two spheres separated by a spacer longer than that used in the individual stages. After firing, the assembly can be navigated out of the body.

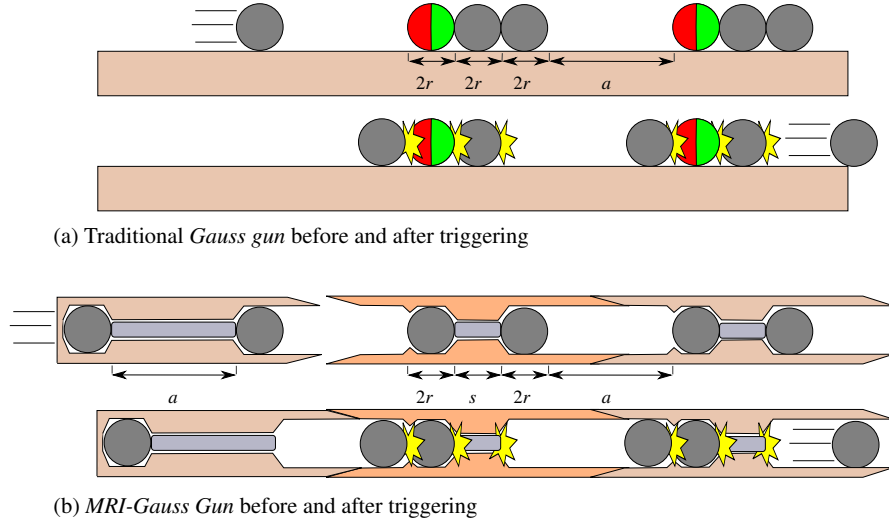


Fig. 11 Operation of a Gauss gun. (a) Standard design for use outside an MRI scanner shown before and after triggering. Magnetized spheres are red and green. Non-magnetized spheres are gray. (b) Design for use inside an MRI scanner shown before and after triggering. All spheres are magnetized when inside scanner. See video at <http://youtu.be/uJ4rFA8x2Js>.

There are four parameters that can be optimized in the design shown in Fig. 11: the sphere radius r , the intra-stage separation s , the inter-stage air gap a , and the number of stages N .

Each component contains two spheres and a separator. Each *barrel* contains a separator of length s and $1/2a$ of material to create an air gap at each end, with a total length of $4r + a + s$. The *trigger* component must have a separator at least as long as a to ensure automatic firing when the *trigger* is attached to another component. The *trigger* also contains connective material to create the air gap $a/2$, giving a total length of $1.5a + 4r$.

Gauss guns are often composed of one or more neodymium magnets and several similarly sized steel spheres. The Gauss guns described in this paper use chrome steel spheres (E52100 Alloy, McMaster 9292K41) for the magnets and shaped rods of nonmagnetic metal for spacers. This provides several benefits:

- inside an MRI, steel is a stronger magnet than neodymium
- spacer length is arbitrary and can be chosen to maximize energy
- leaving multiple magnets in tissue is potentially dangerous, leading, e.g., to bowel necrosis, perforation, volvulus, sepsis, and possible death [?, ?]. In con-

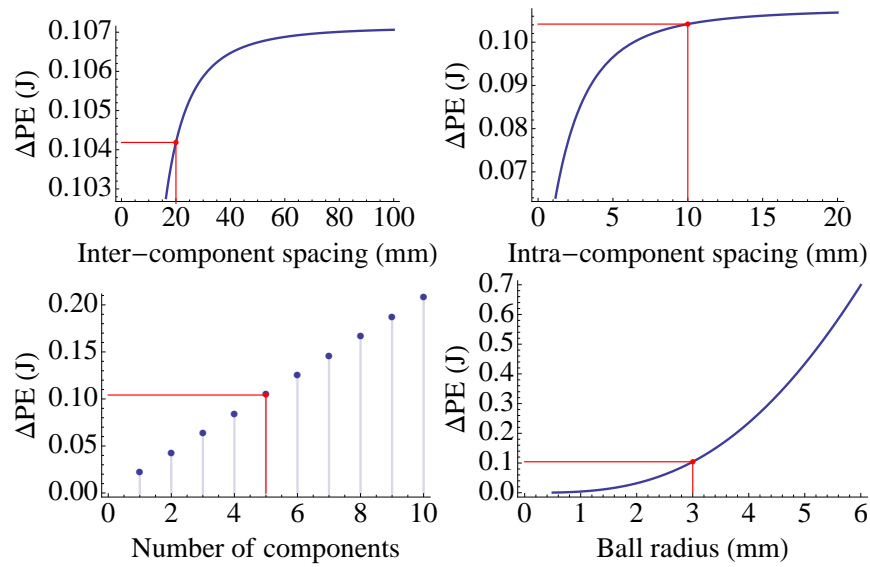


Fig. 12 Potential energy as a function of four design parameters. See design software at [http://demonstrations.wolfram.com/OptimizingAGaussGun/\[?\]](http://demonstrations.wolfram.com/OptimizingAGaussGun/[?]).

trast, the steel bearing balls used in this study lose their magnetism when removed from the magnetic field of the MRI

- MRI enables imaging and control to assemble components at target
- MRI enables controlled removal of components

The prototype Gauss gun components are shown in Fig. ?? . The *barrel* components can be stacked to achieve stronger forces. A *trigger* component fires the Gauss gun. An optional *delivery* component can be used to administer the desired treatment, either a puncture or a drug delivery.

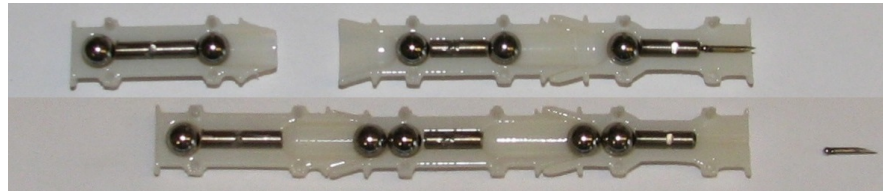


Fig. 13 Cross-section, three component Gauss gun before and after firing.

The E52100 alloy steel spheres are largest weight contributors to the Gauss gun. The separator material must have low magnetic saturation and transmit kinetic energy by having a high coefficient of restitution. Aluminum, tungsten, and titanium are all reasonable replacements, but tungsten is heavy, and aluminum is soft. The

separator need not be the same diameter as the spheres and instead can be a thin rod, further lowering the weight.

Tradeoffs between the parameters are shown in Fig. 12. Potential energy increases with the cube of ball radius, linearly with number of stages, and asymptotically increases to a limit with inter- and intra-component spacing.

Several tests including tissue penetration, self-assembly and MRI tracking were conducted in a Siemen's Skyra 3T clinical MRI scanner. The tests use a brain model composed of a solidified 0.5% agarose gel solution [20]. A 30mm block of agarose was used and placed near the isocenter of a Siemen's Skyra 3T MRI scanner. The delivery component, loaded with either an 18, 20, or 26-gauge needle was placed against the solution. The experiment results are represented in Fig. 14. Five trials were recorded for each needle size. The penetration distance increases as the gauge increases (needle diameter decreases).

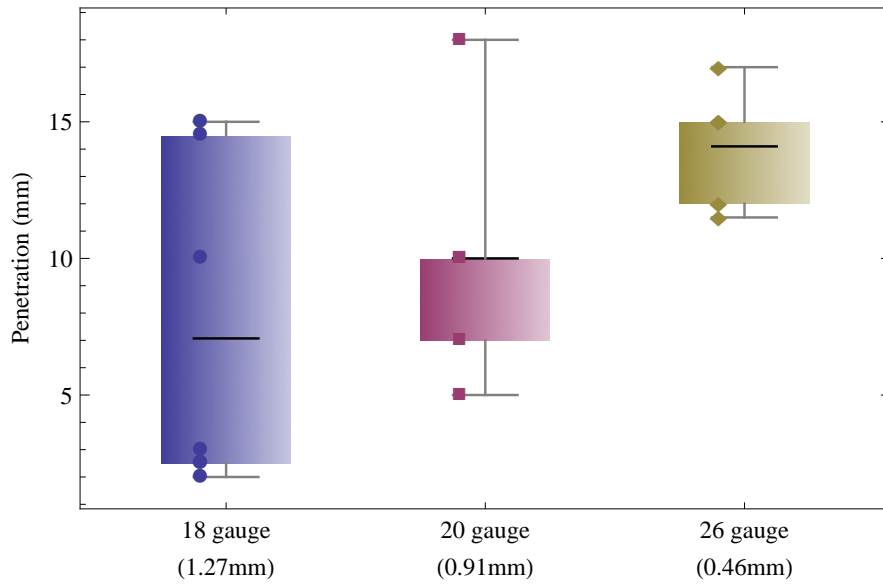


Fig. 14 Penetration of the three needle tips with 1mm sphere shown in Fig. ?? into 5% agar solution, using single-stage MRI Gauss gun.

Figure 16 shows photos from two experiments with Gauss gun assembly and membrane penetration. Three tests were performed, and are included in the video attachment. The first two experiments each used a *delivery* and a *trigger* component and fired 18-gauge needle tips welded to 1mm spheres into a membrane model, a water balloon filled with blue dye. The third experiment tested ranged delivery, by firing the needle projectile using a *delivery*, *barrel*, and *trigger* component to penetrate a membrane model from a distance of 240 mm.

The MRI could provide an integrated environment for intervention using the Gauss gun. Pre-operative and post-operative images could be acquired with the MRI

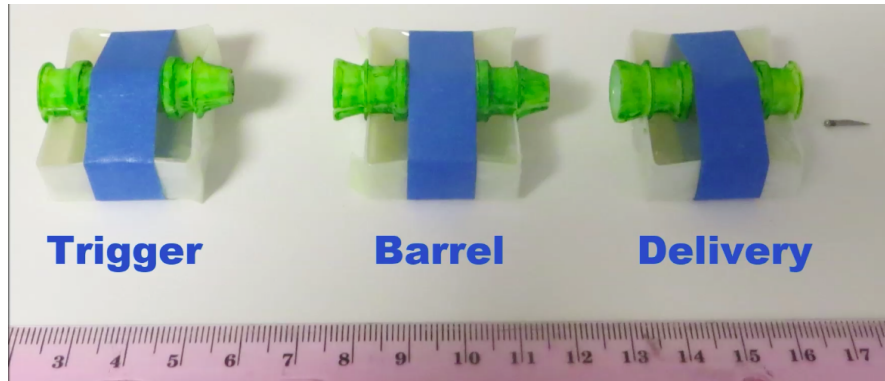


Fig. 15 Gauss gun components used in MRI experiments

as depicted in Fig. 17, showing the membrane model before and after Gauss gun deployment, assembly, and firing. The individual components of the Gauss gun could also be tracked in real-time using RF-selective excitation [?]. Distinct peaks, corresponding to the locations of the Gauss gun components, can be acquired in less than 20ms, as shown in Fig. ??.

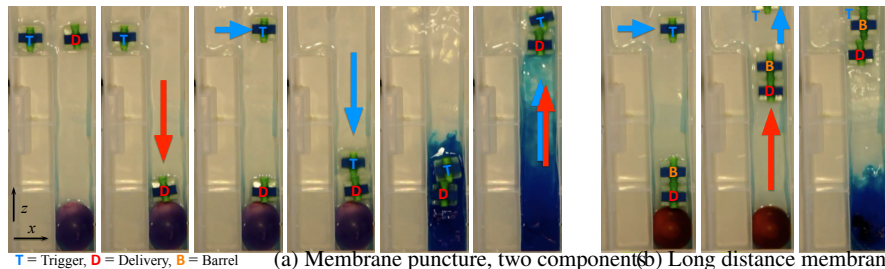


Fig. 16 Photos from an experiment within the MRI bore. The membrane model is a water balloon filled with dye. See the video attachment.

6 Future Directions

Interesting future directions: miniaturization, medical applications, improving tracking and power, etc.

References

1. C. J. Walsh, "Image-guided robots for dot-matrix tumor ablation," Ph.D. dissertation, Massachusetts Institute of Technology, Massachusetts Institute of Technology. Dept. of

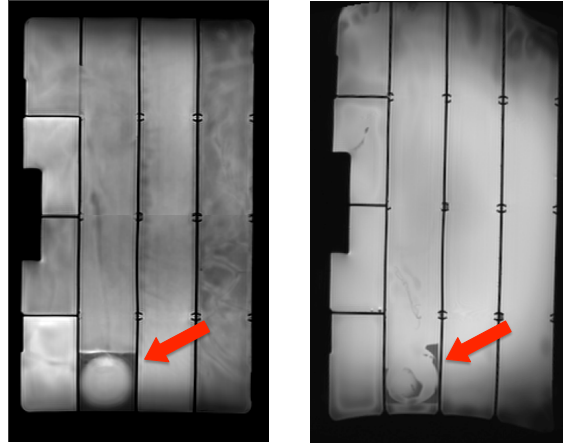


Fig. 17 A T2 weighted Turbo Spin Echo MRI image showing the dye-filled balloon before and after penetration. The agar used to stabilize the balloon is visible in both images.

- Mechanical Engineering., 2010. [Online]. Available: <http://hdl.handle.net/1721.1/61613>
2. M. Ho, A. B. McMillan, J. M. Simard, R. Gullapalli, and J. P. Desai, "Towards a meso-scale sma-actuated mri-compatible neurosurgical robot," *IEEE Transaction on Robotics*, vol. 28, no. 1, pp. 213–222, 2012.
3. G. S. Fischer, A. Krieger, I. Iordachita, C. Csoma, L. L. Whitcomb, and G. Fichtinger, "MRI compatibility of robot actuation techniques—a comparative study," in *Medical Image Computing and Computer-Assisted Intervention—MICCAI 2008*. Springer, 2008, pp. 509–517.
4. S. Martel, J.-B. Mathieu, O. Felfoul, A. Chanu, E. Aboussouan, S. Tamaz, P. Pouponneau, L. Yahia, G. Beaudoin, G. Soulez, and M. Mankiewicz, "Automatic navigation of an untethered device in the artery of a living animal using a conventional clinical magnetic resonance imaging system," *Applied Physics Letters*, vol. 90, no. 11, pp. 114 105–114 105–3, Mar 2007.
5. P. Vartholomeos, L. Qin, and P. E. Dupont, "MRI-powered actuators for robotic interventions," in *IEEE Int. Rob. and Sys.*, 2011, pp. 4508–4515.
6. P. Vartholomeos, C. Bergeles, L. Qin, and P. E. Dupont, "An MRI-powered and controlled actuator technology for tetherless robotic interventions," *Int. J. Rob. Res.*, vol. 32, no. 13, pp. 1536–1552, 2013.
7. R. C. Ritter, M. S. Grady, M. A. H. III, and G. T. Gillies, *Computer-integrated Surgery: Technology and Clinical Applications*. The MIT Press, 1996, ch. 26 Magnetic Stereotaxis: Computer-Assited, Image-Guided Remote Movement of Implants in the Brain, pp. 363–370.
8. A. Chanu, O. Felfoul, G. Beaudoin, and S. Martel, "Adapting the clinical mri software environment for real-time navigation of an endovascular untethered ferromagnetic bead for future endovascular interventions," *Magn Reson Med*, vol. 59, no. 6, pp. 1287–1297, Jun. 2008.
9. P. Vartholomeos, M. Akhavan-Sharif, and P. E. Dupont, "Motion planning for multiple millimeter-scale magnetic capsules in a fluid environment," in *IEEE Int. Conf. Rob. Aut.*, May 2012, pp. 1927–1932.
10. A. Becker, E. Demaine, S. Fekete, and J. McLurkin, "Particle computation: Designing worlds to control robot swarms with only global signals," in *IEEE International Conference on Robotics and Automation (ICRA)*. Hong Kong: IEEE, May 2014, pp. 6751–6756.
11. R. Schill, "General relation for the vector magnetic field of a circular current loop: a closer look," *Magnetics, IEEE Transactions on*, vol. 39, no. 2, pp. 961–967, Mar 2003.
12. Z. Artstein, "Stabilization with relaxed controls," *Nonlinear Analysis*, vol. 15, no. 11, pp. 1163–1170, 1983.

13. J. J. Thomson, "On the structure of the atom: an investigation of the stability and periods of oscillation of a number of corpuscles arranged at equal intervals around the circumference of a circle; with application of the results to the theory of atomic structure," *Philosophical Magazine Series 6*, vol. 7, no. 39, pp. 237—265, Mar. 1904.
14. H. Peng and Y. Yu, "Optimization on the surface of the (hyper)-sphere," Purdue University, Tech. Rep., May 2012. [Online]. Available: <https://www.cs.purdue.edu/homes/pengh/reports/5900P.pdf>
15. A. Becker. (2014, Jan.) "Control n MRI-powered actuators." MATLAB Central File Exchange. [Online]. Available: <http://www.mathworks.com/matlabcentral/fileexchange/45331>
16. W. K. Cho, J. A. Ankrum, D. Guo, S. A. Chester, S. Y. Yang, A. Kashyap, G. A. Campbell, R. J. Wood, R. K. Rijal, R. Karnik, R. Langer, and J. M. Karp, "Microstructured barbs on the north american porcupine quill enable easy tissue penetration and difficult removal," *Proceedings of the National Academy of Sciences*, vol. 109, no. 52, pp. 21 289–21 294, 2012. [Online]. Available: <http://www.pnas.org/content/109/52/21289.abstract>
17. M. Mahvash and P. Dupont, "Mechanics of dynamic needle insertion into a biological material," *Biomedical Engineering, IEEE Transactions on*, vol. 57, no. 4, pp. 934–943, April 2010.
18. J. A. Rabchuk, "The gauss rifle and magnetic energy," *The Physics Teacher*, vol. 41, no. 3, pp. 158–161, 2003.
19. D. Kagan, "Energy and momentum in the gauss accelerator," *The Physics Teacher*, vol. 42, no. 1, pp. 24–26, 2004.
20. I. Howard, M.A. B. Abkes, M. Ollendieck, M. Noh, R. C. Ritter, and G. Gillies, "Measurement of the force required to move a neurosurgical probe through in vivo human brain tissue," *Biomedical Engineering, IEEE Transactions on*, vol. 46, no. 7, pp. 891–894, July 1999.